Absolute prompt-gamma yield measurements for ion beam therapy monitoring

M Pinto[1], M Bajard[1], S Brons[2], M Chevallier[1], D Dauvergne[1], G Dedes[1], M De Rydt[1,3], N Freud[4], J Krimmer[1], C La Tessa[5], J M Létang[4], K Parodi[6,7], R Pleskač[5], D Prieels[8], C Ray[1], I Rinaldi[6,7], F Roellinghoff[1,4,8], D Schardt[5], E Testa[1] and M Testa[1]

[1] IPNL; Université de Lyon, F-69003 Lyon, France; Université Lyon 1, F-69622 Villeurbanne, France; CNRS/IN2P3, UMR 5822 F-69622 Villeurbanne, France
[2] Heidelberg Ion-Beam Therapy Center, Heidelberg, Germany
[3] Instituut voor Kern- en Stralingsfysica, KU Leuven, Celestijnenlaan 200D, B-3001 Leuven, Belgium
[4] CREATIS; Université de Lyon, F-69003 Lyon, France; Université Lyon 1, F-69622 Villeurbanne, France; CNRS UMR 5220; INSERM U1044; INSA-Lyon; Centre Léon Bérard, France
[5] GSI Helmholtzzentrum für Schwerionenforschung, Planckstraße 1, 64291, Darmstadt, Germany
[6] Heidelberg University Hospital, Im Neuenheimer Feld 672, 69120 Heidelberg, Germany
[7] Ludwig Maximilians University, Professor-Huber-Platz 2, 80539 Munich, Germany
[8] Ion Beam Applications SA, Chemin du Cyclotron 3, B-1348 Louvain-la-Neuve, Belgium

E-mail: pinto@ipnl.in2p3.fr

CrossMark

Abstract

Prompt-gamma emission detection is a promising technique for hadrontherapy monitoring purposes. In this regard, obtaining prompt-gamma yields that can be used to develop monitoring systems based on this principle is of utmost importance since any camera design must cope with the available signal. Herein, a comprehensive study of the data from ten single-slit experiments is presented, five consisting in the irradiation of either PMMA or water targets with lower and higher energy carbon ions, and another five experiments using PMMA targets and proton beams. Analysis techniques such as background subtraction methods, geometrical normalization, and systematic uncertainty estimation were applied to the data in order to obtain absolute prompt-gamma yields in

units of prompt-gamma counts per incident ion, unit of field of view, and unit of solid angle. At the entrance of a PMMA target, where the contribution of secondary nuclear reactions is negligible, prompt-gamma counts per incident ion, per millimetre and per steradian equal to $(124 \pm 0.7_{stat} \pm 30_{sys}) \times 10^{-6}$ for 95 MeV u^{-1} carbon ions, $(79 \pm 2_{stat} \pm 23_{sys}) \times 10^{-6}$ for 310 MeV u^{-1} carbon ions, and $(16 \pm 0.07_{stat} \pm 1_{sys}) \times 10^{-6}$ for 160 MeV protons were found for prompt gammas with energies higher than 1 MeV. This shows a factor 5 between the yields of two different ions species with the same range in water (160 MeV protons and 310 MeV u^{-1} carbon ions). The target composition was also found to influence the prompt-gamma yield since, for 300/310 MeV u^{-1} carbon ions, a 42% greater yield $((112 \pm 1_{stat} \pm 22_{sys}) \times 10^{-6}$ counts ion^{-1} mm^{-1} sr^{-1}) was obtained with a water target compared to a PMMA one.

(Some figures may appear in colour only in the online journal)

1. Introduction

Radiotherapy using protons and heavier ions is becoming increasingly widespread. These particles show an energy deposition profile yielding a favourable depth-dose profile to be used in radiation therapy (Schardt *et al* 2010). Such a profile is characterised by the Bragg peak, a narrow and sharp peak located towards the end of the ion path that corresponds to a region where a significant part of the energy is deposited. Since the depth-dose profile of protons and heavier ions allows in principle for a precise local dose distribution, it is of utmost importance to ensure that the dose delivered during the treatment corresponds to the one on the treatment planning. Otherwise, deviations from the treatment plan may produce undesired effects, like e.g. overdosage to the healthy tissue and underdosage to the tumour, if for example ion range shifts occur (Knopf and Lomax 2013).

PET is currently the only particle therapy monitoring technique in clinical application (e.g. Hishikawa *et al* 2002, Enghardt *et al* 2004, Parodi *et al* 2007, Bauer *et al* 2013). It relies on the detection of positron emitters induced by nuclear reactions in the irradiated tissue, which can be correlated with the ion range. Alternative techniques also make use of by-products of the nuclear reactions that occur during irradiation, either prompt gammas emitted by excited nuclei or secondary particles created by inelastic nuclear reactions. The latter was recently suggested by Amaldi *et al* (2010) and is being studied by our collaboration (Henriquet *et al* 2012) as well. It involves the detection of e.g. protons produced by the nuclear reactions of primary carbon ions.

The emission of prompt-gamma rays takes place within less than one nanosecond after nuclear reactions and can be considered to ensue where the nuclear interaction occurs, thus allowing for ion beam range monitoring in real time, provided there are high enough detection statistics. A drawback of this technique is the concurrent emission of prompt gammas resulting from the nuclear reactions undergone by the secondary particles created along the primary ion beam path. This can be more troublesome when using carbon ion beams with higher energies, where a pronounced gamma emission is still present after the fall-off in the prompt-gamma emission profile.

Several designs and concepts resorting to prompt-gamma detection have been proposed for ion beam range monitoring, namely the multi-slit collimated camera (Min *et al* 2006,

Testa *et al* 2008), the Compton camera (Peterson *et al* 2010, Kormoll *et al* 2011, Richard *et al* 2011, Robertson *et al* 2011, Park *et al* 2012), the knife-edge-shaped slit camera (Bom *et al* 2012, Smeets *et al* 2012), the pinhole camera (Kim *et al* 2009), the multi-hole camera (Lee *et al* 2012), the prompt-gamma timing (Golnik *et al* 2014), and the single-slit collimator with energy and time-resolved detection of prompt gammas (Verburg *et al* 2013). Specifically for collimated cameras, studies have shown that it is possible to retrieve information about the ion range in real time both for protons (Min *et al* 2006) and carbon ions (Testa *et al* 2008, Testa *et al* 2009). Such a camera aims at detecting only the gammas emitted with an approximately right angle with respect to the beam axis. The rationale for this angular selectivity was discussed by Testa *et al* (2009), who found no relevant anisotropicity of the emitted gammas. Thus, the said angular constraint allows for the use of the optimum longitudinal range correlation. Nevertheless, the emission of prompt gammas is also accompanied by the emission of neutrons, thus the application of discrimination methods has been suggested for carbon ion therapy prompt-gamma monitoring (Testa *et al* 2008, Testa *et al* 2009) and is desirable for the case of proton therapy (Roellinghoff *et al* 2014). The use of time of flight (TOF) considerations was proposed by Testa *et al* (2008) and makes it possible to discriminate the prompt-gamma signal from neutrons and neutron-associated components, such as neutron-induced gammas produced in the collimator and shielding material. The same work has also shown that including an energy threshold in the prompt-gamma detection analysis would further improve the signal-to-background ratio (SBR).

Every ion range verification method presented above relies on having a predictable spatial distribution of the respective observable to compare with the measured one. In this context, Monte Carlo codes are usually employed to simulate the interactions of particles with matter. However, their use may introduce additional uncertainties since there are no well-established theoretical models to predict nuclear interactions (Seravalli *et al* 2012). In addition, discrepancies between the prompt-gamma emission prediction for proton and carbon ion beams using Geant4 (Agostinelli *et al* 2003) and experimental data have been reported (Le Foulher *et al* 2010, Verburg *et al* 2012, Polf *et al* 2014). Recently, Espa na *et al* (2011) and Seravalli *et al* (2012) have also addressed this issue for PET monitoring in a proton irradiation scenario.

A set of experiments using single-slit collimated detectors and the corresponding data analysis are presented herein. The main goal is to obtain absolute yields for prompt-gamma emission using both proton and carbon ion beams in the context of hadrontherapy monitoring. Henceforth, absolute yields will be referred to as the description of the prompt-gamma signal in units of prompt-gamma counts per incident ion, unit of field of view (millimetre), and unit of solid angle (steradian). These yields will also be corrected for the detector efficiency and for the prompt-gammas able to cross the collimator material and shielding. The rationale for the analysis here presented is to gather experimental data appropriate for comparison with simulations and to cross-check such data with other experimental designs. Ultimately, all of these experiments and data analyses are crucial for any quantitative use of the information provided by the prompt-gamma emission, namely to guide the construction of a clinical prompt-gamma camera prototype and to predict the prompt-gamma distributions to be used as a reference during the treatment.

The experiments are described in detail in section 2 and the results of a sequential procedure to achieve absolute yields are shown in section 3.

2. Materials and methods

In this section ten experiments using single-slit collimated detectors are described. For the sake of simplicity, henceforth experimental data resulting from one detector will be considered as

a single experiment. There are some cases for which two detectors were used in parallel in the same measurement but they will undergo independent analysis.

Two of the experiments were carried out at the Grand Accélérateur National d'Ions Lourds (GANIL, Caen, France), another two at the GSI Helmholtzzentrum für Schwerionenforschung (GSI, Darmstadt, Germany), one at the Heidelberger Ionenstrahl-Therapiezentrum (HIT, Heidelberg, Germany), and the five remaining at the Westdeutsches Protonentherapiezentrum Essen (WPE, Essen, Germany). All the experiments listed were performed using carbon-ion beams, except the ones at WPE, where proton beams were employed.

Some of the experimental data of two of these experiments have already been published by our collaboration (Testa *et al* 2009, Testa *et al* 2010). However, they are included in this work and subjected to a different analysis in order to test their consistency with respect to absolute yields.

2.1. Common features of the experimental setups

Before describing each experiment in detail, the common features to all of them are outlined. First, the detection of the prompt gammas emitted from the different targets was performed in all cases at approximately right angles with respect to the beam axis, and using the TOF technique to improve the contrast between the signal and the background, as already demonstrated by Testa *et al* (2008), thus providing the possibility to discriminate the prompt-gamma events from the background. The time window applied to select the prompt-gamma signal is intrinsically linked to the detector used for each experiment and its time resolution. Herein, the results obtained with five different detectors are presented: a cylindrical thallium-doped sodium iodide [NaI(Tl)] detector with 3 inch diameter and 3 inch length, an hexagonally-shaped barium fluoride (BaF_2) detector with 50 mm edge and 140 mm length, two cerium-doped lutetium-yttrium oxyorthosilicate (LYSO:Ce) detectors with $50 \times 40 \times 3$ mm^3 and $50 \times 40 \times 5$ mm^3, and a cerium-doped lanthanum(III) bromide ($LaBr_3$:Ce) detector with 1 inch diameter and 2 inch length.

Another common feature to this set of experiments was the use of a VME-based acquisition system with NIM modules and conventional electronics, which was triggered by the OR logical signal of the detectors. An event-by-event acquisition mode was set to allow for TOF information to be stored, thus the trigger was used as the TOF start signal. The TOF stop signal in the carbon ion beam experiments was given by a suitably delayed signal, either by a detector intercepting the primary beam or by the high-frequency (HF) signal of the accelerator. In turn, in the proton beam experiments the TOF stop signal was given by the HF signal of the accelerator. The stop signal was actually provided by a discriminator converting the HF signal into a digital logic signal whose frequency was divided by a factor of ~5 with respect to the HF frequency to cope with the time-to-digital converter (TDC) module limitations. The TOF spectra measured in these conditions correspond therefore to ~5 periods of the HF signal (see figure 1). Dead time correction was applied based on the data from the scalers used during each experiment.

The targets were placed on top of a moving table and acquisitions were carried out at different positions, while the collimator, the shielding and the detectors remained in a fixed position. Afterwards, the events within a region of each measured TOF spectrum (i.e. the time window) were summed to obtain the corresponding yield. The width of the time window is sufficiently large to include all the observable signal. A summary of the detectors and time windows used in each experiment is given in table 1.

Although an absorbed energy threshold of 2 MeV is close to the optimum to enhance the contrast of the prompt-gamma signal for some of the experiments as already suggested
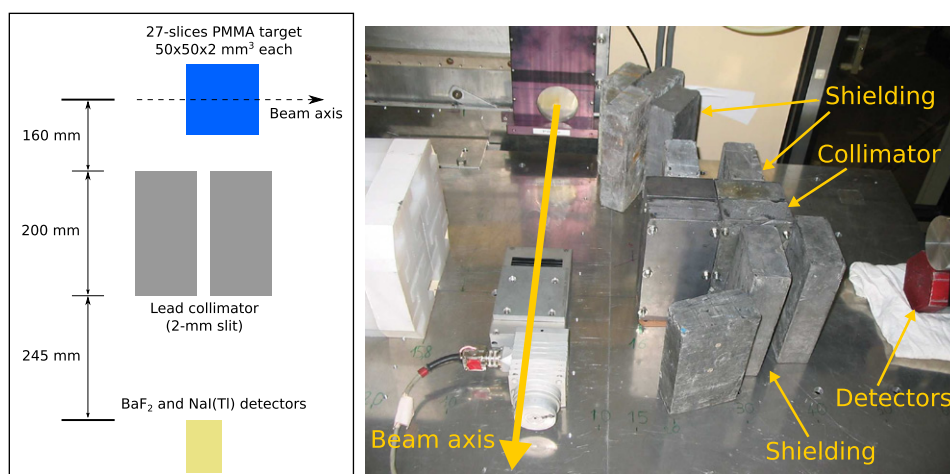
Figure 1. A schematic illustration (left) and a picture (right) of the GANIL 95 MeVu^{-1} ^{12}C^{6+} experiments. It should be noted that the target is not shown in the picture and that the schematic illustration is not to scale.

Table 1. Values of the width of the time window used for the TOF analysis of each experiment.

Experiment	Detector	Time window (ns)
GANIL 95 MeV u^{-1} ^{12}C^{6+}	BaF$_2$	2.0
	NaI(Tl)	4.0
GSI 300 MeV u^{-1} ^{12}C^{6+}	BaF$_2$	4.5
GSI 310 MeV u^{-1} ^{12}C^{6+}	BaF$_2$	3.0
HIT 310 MeV u^{-1} ^{12}C^{6+}	LYSO:Ce	3.0
WPE 160 MeV H$^+$ (I)	LYSO:Ce	3.0
	LaBr$_3$:Ce	3.0
WPE 160 MeV H$^+$ (II)	LYSO:Ce	3.0
	LaBr$_3$:Ce	3.0
WPE 160 MeV H$^+$ (III)	LaBr$_3$:Ce	4.0

elsewhere (Testa *et al* 2010), it was decided to opt for a 1 MeV threshold for all the experiments. This was due to the low statistics obtained for some experiments, where a 2 MeV energy threshold would lead to a reduced statistical significance of the signal. Even though the contrast is enhanced, the use of a threshold also entails discarding some of the signal events, which is critical when the statistics are low. Being consistent in this selection allows for a comparison between data sets. Furthermore, in order to use all the data from the different experiments in an equivalent manner, an upper energy threshold was also considered and set to 7 MeV. The energies considered here were obtained after calibration with Na-22 (0.511 and 1.275 MeV), Co-60 (1.1732 and 1.2325 MeV) and/or Cs-137 (0.662 MeV) sources (one or more sources were used in each experiment considering that at least two gamma peaks are available for calibration). It is therefore an absorbed gamma-equivalent energy but, for the sake of simplicity, it will be simply referred to as energy. It is known that scintillator detectors do not have a linear response at higher energies (Agodi *et al* 2012). However, no correction was made to account for this factor since, on the one hand, at energies up to that of the lower

Table 2. Fraction of prompt gammas with energies above 1 MeV, between 1 and 2 MeV, and above 7 MeV. Results obtained by simulation with Geant4 and considering the energy spectrum of the photons escaping the target for each experiment.

Experiment	Fraction above 1 MeV (%)	Fraction between 1 and 2 MeV (%)	Fraction above 7 MeV (%)
GANIL 95 MeV u^{-1} ^{12}C^{6+}	49.6	11.0	9.4
GSI 300 MeV u^{-1} ^{12}C^{6+}	33.7	7.7	4.5
GSI 310 MeV u^{-1} ^{12}C^{6+}	33.3	7.5	4.3
HIT 310 MeV u^{-1} ^{12}C^{6+}	33.2	8.4	5.2
WPE 160 MeV H$^+$	39.1	8.8	2.1

Table 3. Projected ion ranges estimated by SRIM 2013 (Ziegler *et al* 2008).

Experiment	Target	Projected ion range (mm)
GANIL 95 MeV u^{-1} ^{12}C^{6+}	PMMA	20.99
GSI 300 MeV u^{-1} ^{12}C^{6+}	Water	174.05
GSI 310 MeV u^{-1} ^{12}C^{6+}	Water	1.2.78
HIT 310 MeV u^{-1} ^{12}C^{6+}	PMMA	1.2.49
WPE 160 MeV H$^+$	PMMA	154.72

threshold the response is expected to be linear and, on the other hand, the fraction of events above 7 MeV is small (*vide* table 2). In consequence, the impact on the results of any possible inaccuracy in selecting exactly 7 MeV is likely to be marginal. In fact, for the present work the energy information is not important apart from event-selection purposes. Therefore, even if the detector response in the energy selection window (1–7 MeV) is not linear, the crucial point is the selection of the events to be considered for the subsequent TOF analysis. In any case, an uncertainty around the 7 MeV threshold cannot be excluded, but its impact is quite small due to the reduced number of events in this energy region. Likewise, the use of this high energy threshold should yield a small influence in the absolute yield values presented herein. Table 2 shows the fraction of prompt gammas escaping the target above 1 MeV and between 1 and 2 MeV obtained with Monte Carlo simulations and using the setup of each experiment. This table presents the energy of prompt gammas escaping the target and, thus, if no other interactions occur during the photon path, it shows the different energy fractions of incident prompt gammas in the detectors. Therefore, these data cannot be directly compared with the experimental data since some photons may have undergone Compton scattering and escaped the detectors, hence not depositing their full energy. However, these numbers are physically more relevant because they give insights about the (simulated) energy distribution of prompt gammas. Moreover, if one considers the escaping photons in the detectors, the fraction about 7 MeV will be smaller, so confirming the marginal issue of having the high energy threshold.

Although the nominal particle energy of each experiment is shown, it should be stressed that, in several experiments, detectors were placed in the beam path upstream of the target in order to normalise the data to the number of ions. Hence, the real ion range in the target should correspond to a different particle energy. Table 3 shows the projected ion ranges estimated by SRIM 2013 (Ziegler *et al* 2008) assuming the nominal particle energy in the target.

Throughout the present work Monte Carlo simulations are used. These simulations were performed using Geant4 9.6.p02.

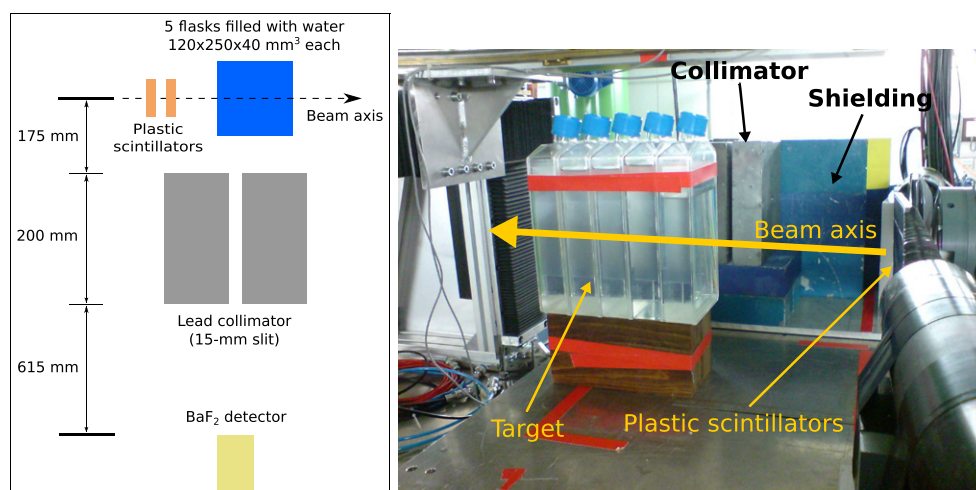A summary of the experimental details can be found in table A1 (appendix A).

Figure 2. A schematic illustration (left) and a picture (right) of the GSI 300 MeVu^{-1} ^{12}C^{6+} experiment. It should be noted that the detector is not visible in the picture and that the schematic illustration is not to scale.

2.2. GANIL 95 MeV u^{-1} ^{12}C^{6+}

The BaF$_2$ and the NaI(Tl) detectors were positioned alongside with some additional lead shielding at 605 mm from the beam axis. A 200 mm-thick lead collimator with a 2 mm slit was placed between the detector and the target, which consisted of 27 PMMA slices of $50 \times 50 \times 2$ mm^3 each. The monitor for the number of incident ions consisted of a small NaI(Tl) detector placed at a defined distance from the experimental setup and calibrated against a Faraday cup. The influence of the target position on the dose monitor was also checked and it was found to be less than 1% . Nevertheless, the calibration was corrected for this factor. The time structure of the cyclotron at GANIL allowed for the use of the HF signal as TOF stop signal (pulsed beam with a pulse width of approximately 1 ns every 80 ns). The circular beam full-width at half maximum (FWHM) spot size was found to be approximately 5 mm at the target position.

A schematic illustration and a picture of these experiments can be observed in figure 2. Further illustrations, pictures and a more detailed description are presented elsewhere (Testa *et al* 2010).

2.3. GSI 300 MeV u^{-1} ^{12}C^{6+}

The BaF$_2$ detector was also used in this experiment. It was positioned at 990 mm from the beam axis. A 200 mm-thick lead collimator with a 15 mm slit was placed between the target and the detector. Some lead shielding was added around the detector and the collimator to improve the SBR. A target composed of five plastic flasks filled with water was used. Each flask had dimensions of $120 \times 250 \times 40$ mm^3. Special care was taken in preventing spaces between flasks. Although no measurement upstream or downstream of the target was made for this experiment, one with a closed collimator was performed. The TOF stop signal was provided by a delayed signal coming from two plastic scintillators intercepting the beam. To avoid losing ion triggering in the plastic scintillators, the beam intensity was kept at low values
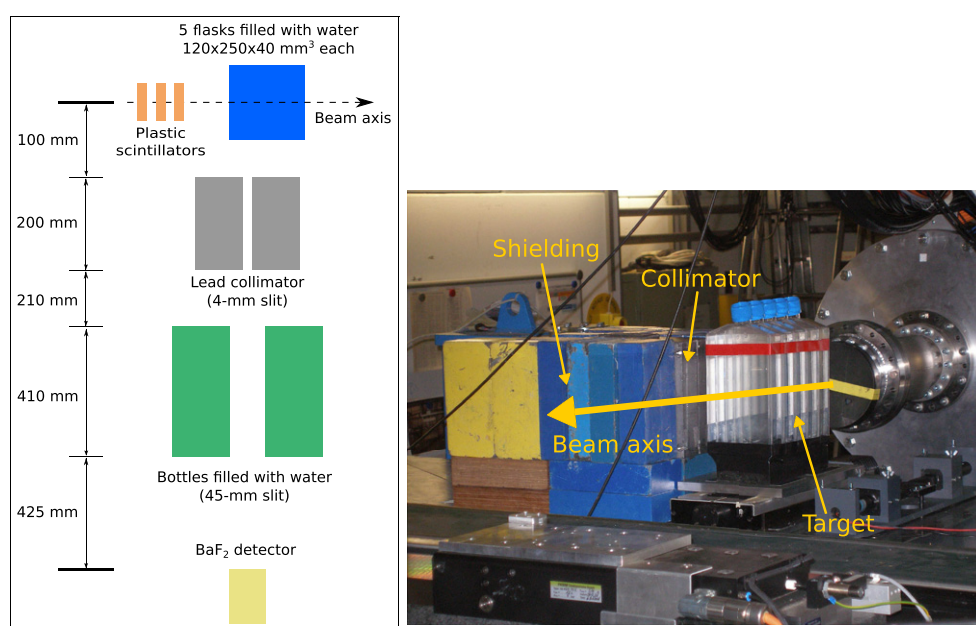
Figure 3. A schematic illustration (left) and a picture (right) of the GSI 310 MeVu^{-1} ^{12}C^{6+} experiment. It should be noted that the detector is not visible in the picture and that the schematic illustration is not to scale.

(i.e. up to a few 10^5 ions s^{-1}). However, if an incident ion was missed and its secondary radiation was registered, it would not be taken into account afterwards during the analysis due to the TOF information. These detectors also allowed for retrieving the number of ions hitting the target, thus providing the normalization factor. An ionization chamber (IC) was also used to cross-check the normalization factor provided by the plastic scintillators. The synchrotron at GSI was set to a continuum extraction mode (approximately 8 s extraction every 10 s) with an elliptical FWHM spot size of *ca*. 13 mm and 10 mm at the target position, respectively for the *Y*- and the *X*-axis and considering the beam direction as the *Z*-axis.

A schematic illustration and a picture of this experiment can be observed in figure 3.

2.4. GSI 310 MeV u^{-1} ^{12}C^{6+}

This experiment employed the same detector, target and normalization procedure with the information provided by plastic scintillators and an IC, as in the GSI 300 MeV u^{-1} ^{12}C^{6+} one (*vide* section 2.3). However, the setup was different. In this case the BaF$_2$ detector was positioned at a distance of 1345 mm from the beam axis with a 200 mm-thick lead collimator between the target and the detectors. The collimator had a slit of 4 mm. Some lead shielding was added to the setup and several water containers were placed between the collimator and the detector in order to provide shielding against neutrons.

A schematic illustration and a picture of this experiment can be observed in figure 4. The corresponding data analysis has already been published elsewhere (Testa *et al* 2010) along with further illustrations, pictures and additional description of this experiment.
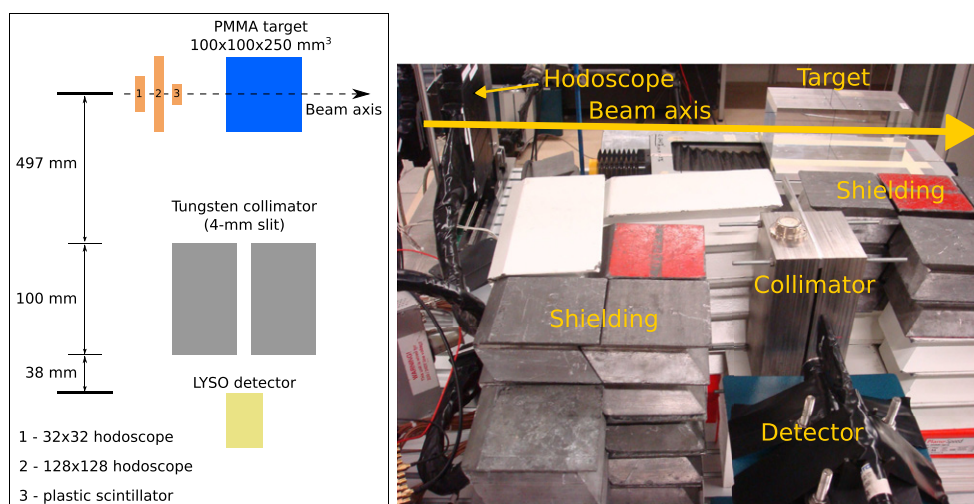
Figure 4. A schematic illustration (left) and a picture (right) of the HIT 310 MeVu^{-1} $^{12}C^{6+}$ experiment. The schematic illustration is not to scale.

2.5. HIT 310 MeV u^{-1} $^{12}C^{6+}$

A LYSO:Ce detector with $50 \times 40 \times 5$ mm^3 was positioned at 635 mm from the beam axis. A tungsten-alloy collimator with thickness of 100 mm and a slit of 4 mm was used. Additional lead shielding was placed surrounding the detector and the collimator. The target was a $100 \times 100 \times 250$ mm^3 PMMA phantom positioned on top of a moving table. The TOF stop signal was given by a suitably delayed signal coming from a plastic scintillator intercepting the beam after the beam exit. During this experiment a beam hodoscope being developed in-house was also positioned after the beam exit and hence an additional loss in the beam energy is expected. The beam FWHM spot size was found to be approximately 3.8 mm at the target position.

A schematic illustration and a picture of this experiment can be observed in figure 5.

2.6. WPE 160 MeV H$^+$ (I)

For these experiments the LaBr$_3$:Ce and the $50 \times 40 \times 3$ mm^3 LYSO:Ce detectors were used. They were placed at 600 mm from the beam axis behind a tungsten-alloy collimator, which had a slit of 4 mm, and some lead shielding. The LaBr$_3$:Ce detector was placed on top of the LYSO:Ce. The target used was a cylindrical PMMA phantom with 75 mm radius and 200 mm length. The TOF stop signal was given by the HF of the cyclotron running in pulsed mode with a time structure of approximately 1 ns pulse (FWHM) every 10 ns. The circular beam spot was around 5 mm sigma at isocentre, considering a Gaussian spatial beam distribution (Grevillot *et al* 2011).

The number of incoming protons was given by the IC placed inside the beam nozzle and by the monitor unit (MU) system. An MU is a measure of the dose being delivered after calibration of the IC inside the beam nozzle under reference conditions. Although the MU system relies on the IC for its calibration, it was used as a second system able to cross-check the results. In turn, the IC was calibrated against a Bragg peak chamber positioned at the target entrance.

A schematic illustration and a picture of these experiments can be observed in figure 6.
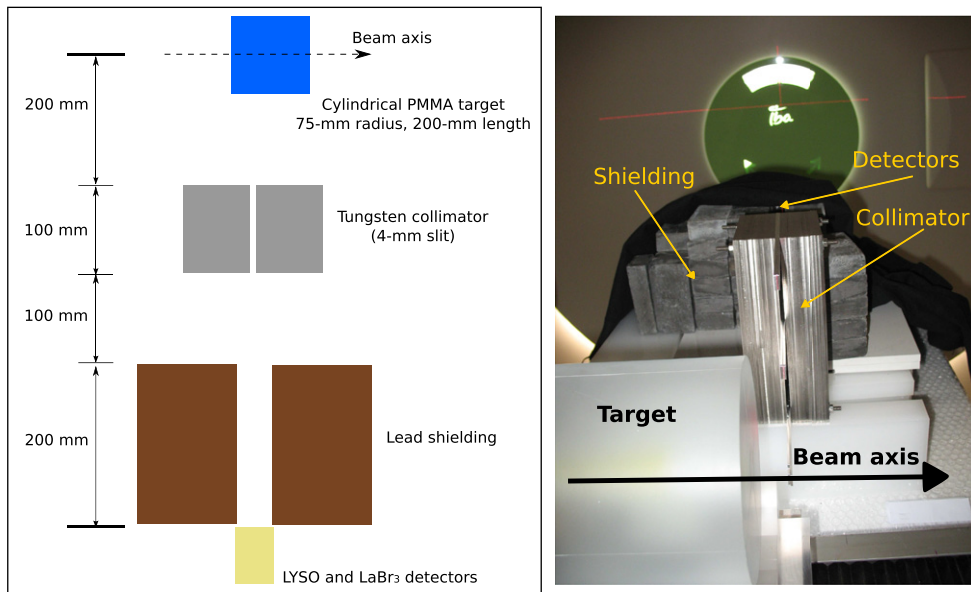
Figure 5. A schematic illustration (left) and a picture (right) of the WPE 160 MeV (I) protons experiments. The schematic illustration is not to scale.
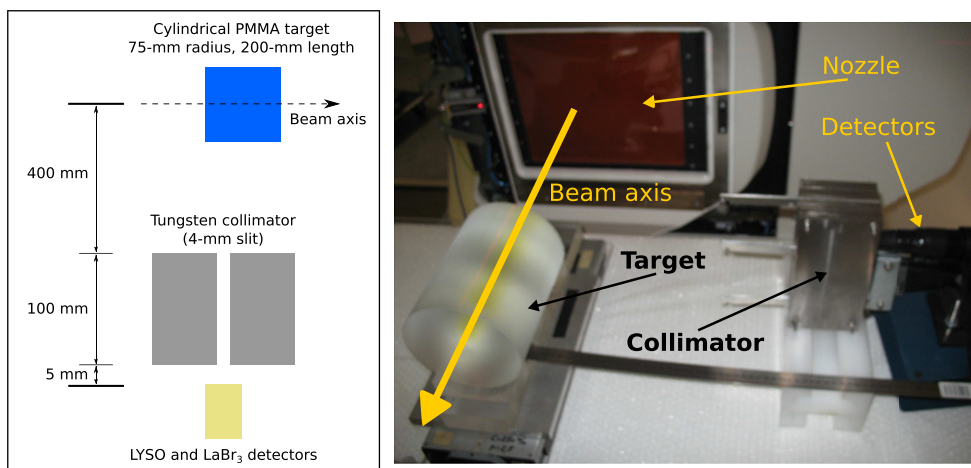

Figure 6. A schematic illustration (left) and a picture (right) of the WPE 160 MeV (II) proton experiments. The schematic illustration is not to scale.

2.7. WPE 160 MeV H⁺ (II)

Following the WPE 160 MeV H^+ (I) experiments, further experiments were conducted with the same $LaBr_3$:Ce and LYSO:Ce detectors but with a different setup. In this setup no lead shielding was used and the detectors were closer to the target. A schematic illustration and a picture of these experiments can be observed in figure 7.
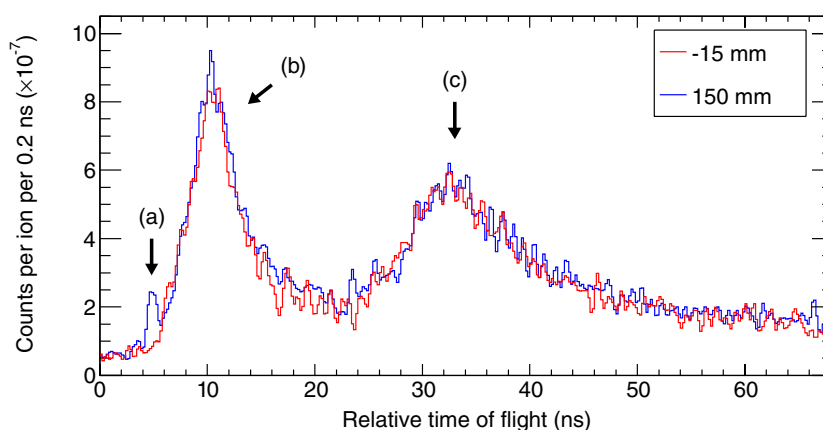
Figure 7. TOF spectra of the GSI 310 MeV u^{-1} ^{12}C^{6+} experiment for the measurement points at −15 mm (upstream of the target) and 150 mm (inside the target). The TOF components corresponding to the events associated with prompt gammas (a), secondary-induced events from the target ((b), mainly neutron-associated events), and events associated with the surroundings ((c), e.g. walls, ceiling) are pointed out by arrows and have been suggested by Testa *et al* (2010). The *X*-axis is relative since no calibration for the axis origin was performed.

2.8. WPE 160 MeV H⁺ (III)

This experiment was performed in different conditions from those of the previous ones (i.e. it was an independent experiment and it took place in a different treatment room). The setup used was similar to the one of WPE 160 MeV H⁺ (II) with the LaBr$_3$:Ce detector, with the exception of the target, which was 50 mm longer in this case.

2.9. Background subtraction

The use of TOF helps in removing most of the background by selecting with a TOF window only the region of interest where the prompt-gamma signal is. Nevertheless, some background events are also present inside the TOF window. One could develop a method based on Monte Carlo simulation in order to estimate the number of those events. However, it is doubtful that simulations could yield enough accuracy in such a case since it is virtually impossible to implement a full description of a complex experiment. Some details are omitted either for simplification (e.g. description of the beam nozzle) or due to unknown parameters (e.g. material composition, distribution of all elements in a room).

Our approach is therefore based solely on experimental data. Two different methods were used according to the ion species. Regardless of the two methods and since a fragmentation tail is not expected for the low energy carbon ion (i.e. 95 MeV u^{-1}) and proton experiments, a linear fit is applied using the points upstream of the target and after the ion range. This linear fit is used to further subtract events from the profile after the background subtraction procedures detailed hereafter. The errors on the fit are also taken into consideration (summed quadratically with the error bars of the data points).

2.9.1. Carbon ion irradiation data. The analysis of these data presented some challenges. On the one hand, the signal (component (a), figure 8) is overlapping with the background in a time
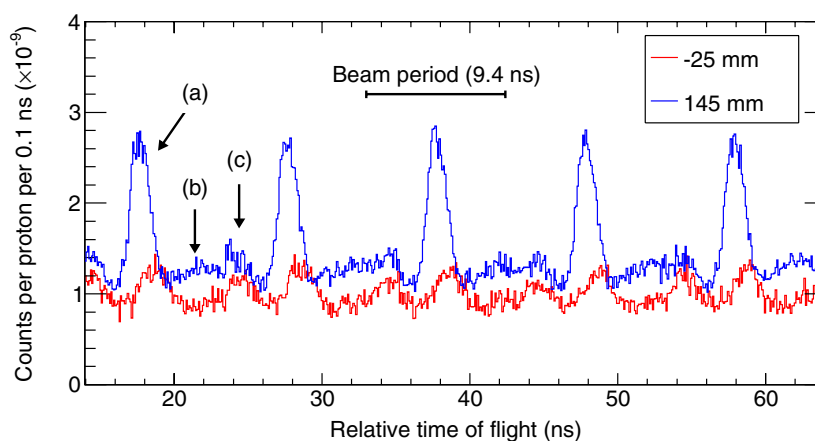
Figure 8. Comparison between two TOF spectra obtained for two longitudinal positions (25 mm upstream of the target and 1.2 mm inside the target). These data come from the WPE 160 MeV H$^+$ (II) experiment using the LaBr$_3$ detector and they include five proton bunches (9.4 ns beam period). The prompt-gamma events (a), the secondary-induced events (b), and the events originated in the nozzle (c) are pointed out by arrows. The nozzle-related events in these data have been already discussed by Pinto *et al* (2014). The *X*-axis is relative since no calibration for the axis origin was performed.

region where the number of events coming from reactions with fast neutrons (component (b), figure 8) is rapidly increasing. This poses some problems mainly in longitudinal positions for which the signal is weaker. On the other hand, the statistics for most of the data with carbon ions are low due to the methods used for the TOF measurement (i.e. when plastic scintillators were used they required a relatively low beam intensity to avoid pile-up). The only exception is the GANIL data for which a different method allowed for a much higher beam intensity at the cost of some loss in accuracy that will be imparted to the data as systematic uncertainty. Figure 8 gives an example of TOF spectra obtained with a 310 MeV u^{-1} carbon-ion beam and the relatively large BaF$_2$ detector: the prompt-gamma peak located around a relative TOF of 5 ns is small as compared to the secondary-induced events coming from the target (component centred at around 10 ns).

The analysis of the data suggests that the background shape in the TOF spectra is the same for every longitudinal position and only its magnitude changes. Such indications were already published by Testa *et al* (2010). For example, a higher background (even if only slightly higher) is expected at the very end of the target rather than at the beginning, since neutron emission is not isotropic and favours forward angles (Gunzert-Marx *et al* 2008, Robert *et al* 2013). As a consequence, a spectrum without prompt-gamma signal can be set as reference and used to subtract the background to the spectra containing both signal and background. The condition for this method to work is the application of a scaling factor to the said reference TOF spectrum that reflects the change in the magnitude of the background along the target depth. This factor is estimated based on the ratio of the integrals outside the TOF window for both the reference spectrum and the one to be subtracted.

For most experiments, the reference TOF spectrum was then set to be the one corresponding to a measurement upstream of the target with the use of adequate collimation and shielding. The only exception was the GSI 300 MeV u^{-1} ^{12}C^{6+} data for which there was no measurement upstream of the target. For this case a closed-collimator configuration was used as reference.

2.9.2. Proton irradiation data. The proton data do not have the issues seen with the carbon ion irradiation. There are both a very distinctive prompt-gamma peak easily separated from the background, and very high statistics since it was not necessary to limit the beam intensity to tag the incident protons for TOF measurement due to the use of the cyclotron HF as STOP signal. Consequently, it was possible to use a more conventional approach by resorting to an already available ROOT (Brun and Rademakers 1997) class calledTSpectrum. Moreover, the background shape on the TOF spectrum changes along the longitudinal position of the scan. Hence, the assumption used for the carbon ion experiments concerning background shape does not hold for this case. Although further studies must be performed to give a definitive answer as to why this happens, it may be related to the fact that the neutrons that are responsible for most of the background are emitted by the target nuclei during proton irradiation, while they mainly come from incident ions with carbon-ion irradiation. The TOF spectrum of neutron-related events with proton irradiation may be therefore more sensitive to target position than in the carbon-ion case.

An example of TOF spectra can be seen in figure 1, where ∼5 periods of the HF signal (since the frequency of the TOF stop signal was divided by a factor of ∼5 with respect to the HF frequency) can be seen. It is possible to observe the distinct shapes of the background in the TOF spectra of a position upstream of the target and at 1.2 mm in the target. Another remark concerns the different prompt-gamma peak positions in the TOF spectrum with respect to distinct longitudinal positions. It can be correlated with the different distances travelled by the protons due to both the movement of the moving table and the longitudinal position in the target being measured as already shown by Biegun *et al* (2012). Such a shift on the prompt-gamma peak is not clearly observed in the carbon ion experiments due to two combined phenomena related to statistics and signal to background ratio. On the one hand, the experiment that provides the highest statistics (i.e. GANIL 95 MeV u^{-1} ^{12}C^{6+}) was performed with small ion ranges, which entails small changes of the moving table to scan the prompt-gamma profile and therefore small shifts on the prompt-gamma peak position. On the other hand, the carbon ion experiments have an important level of background that may hide the time difference since the signal is less visible.

Although retrieving the signal from protons TOF spectra is easier than from carbon ions TOF spectra, there is no procedure capable of telling if after a fitting procedure only prompt-gamma events remain or if some signal was incorrectly subtracted. To address such an issue, it was decided to vary the input parameters of the routineTSpectrum in order to have a set of functions made with different conditions that should be good estimations of the background. This routine is mainly used for gamma spectroscopy applications to determine the background and the location of the discrete gamma peaks. However, it is also well suited for the estimation of the background for the present application. The algorithm considers a clipping window that should correspond to at least approximately the FWHM of the peak. Inside this window, the algorithm assigns to each bin the average value between the bin before and after, or it keeps the same value (the lesser of the two cases). This method is repeated several times and, in the end of this iteration, an estimation of the background is available. In addition, the direction of the iterative process can be increasing (lower to higher values in *X*-axis) or decreasing (higher to lower values in *X*-axis). Before applying this routine, it is also possible to smooth the spectrum to improve the results when significant fluctuations are present. Three input parameters were then varied: smoothing of the histogram (without or with a third-order filter), clipping window direction (either increasing or decreasing), and clipping window width (between 20 and 60 bins). Such parameters and their variation yielded the most meaningful background subtraction after a preliminary study focused on testing this routine. An histogram with the counts retrieved after each fit is built. Finally, the average of this distribution is used as the

number of prompt-gamma events inside the TOF window and the corresponding standard deviation is imparted to the data as systematic uncertainty. Additional information about theT-Spectrum method can be found elsewhere (Morháč *et al* 1997).

2.10.Geometrical normalization

The geometrical parameters of each experiment should be taken into account in order to obtain absolute yields. The parameters that play a role are related to the positioning of each element in the experimental setup and also to other conditions (e.g. collimator slit width). The process for obtaining such parameters to normalise the yields using analytical means is not straightforward. This being so, a Monte Carlo procedure was employed, which allowed us to take into consideration the scattering of photons, the collimator absorption and attenuation coefficients, as well as the shadowing effects around the edges of the collimator slit.

For each experiment and detector three parameters were calculated: the detection field of view (FOV), the detection solid angle and a correction factor accounting for the events able to cross the collimator and the shielding and reach the detectors. The simulated energy spectra of the photons escaping the different targets was used as input.

Each photon emitted isotropically along a line source is propagated across the simulated experimental setup and if the total energy deposition in the detector is within the energy thresholds used for the experimental data, the axial position z of the emission point is registered in order to build a histogram. Figure 9 depicts an ideal case of such a photon emission profile. The line sources had dimensions corresponding to the ion range for each case. A possible definition of the FOV is the FWHM of this distribution (as shown in (1)). In order to keep the detection efficiency constant inside the FOV, it is assumed that the events outside the FWHM (red region in figure 9) are included in this distribution (grey region in figure 9), thus approximating this distribution to a rectangular function.

$$\text{FOV} \approx \text{FWHM} = |z_5 - z_3| \tag{1}$$

In turn, the total detection efficiency ε_{att} is estimated using (2) and it includes the attenuation in the target and the geometrical and intrinsic efficiencies. The calculation consists in considering an isotropic point-like source centred in front of the slit and inside the experimental target, where N_d and N_e are the number of detected and emitted gammas, respectively. The energy distribution of this source was previously estimated by scoring the energy spectrum of the prompt gammas created after either proton or carbon ion irradiations depending on the experiment. In addition, if the energy spectrum of the prompt gammas which are able to escape the target is considered and new simulations with this different energy distribution and without a target are launched, it is possible to define the parameter ε that does not directly consider the attenuation in the target but only the energy distribution of the escaping prompt gammas. In order to estimate the yields for emitted energies above 1 MeV, only gammas with energies above this threshold are considered. Consequently, N_d accounts solely for events that have an energy deposition between 1 and 7 MeV in the detector (i.e. the experimental energy thresholds).

$$\varepsilon_{\text{att}} = \frac{N_{d_{[1 \leqslant E \leqslant 7\text{MeV}]}}}{N_{e_{[E \geqslant 1\text{MeV}]}}} \tag{2}$$

With these considerations, the final absolute yields correspond to absolute yields of prompt gammas with energy higher than 1 MeV.

Finally, the correction factor κ is the ratio between detected events from inside the FOV and all detected events. It estimates the ratio of prompt gammas being observed inside the signal
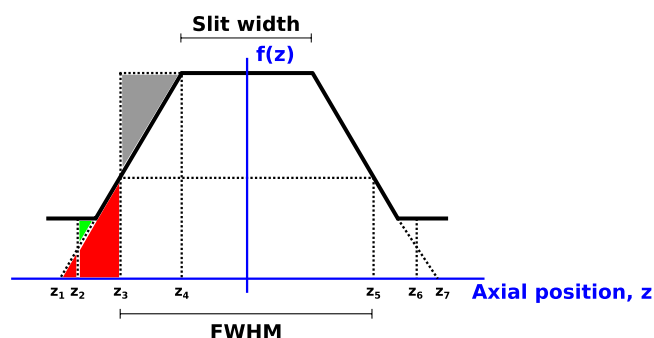
Figure 9. Ideal case of longitudinal distribution of emitted photons after detection in a single-slit experiment.

peak that corresponds to events coming from the slit opening. The photons able to cross the collimator and shielding, thus originating from a different longitudinal position than the one being observed can be obtained through the relationship $(1 - \kappa)$. However, due to the approximation to a rectangular function, κ cannot be estimated using the FOV as presented in (1) since events outside the FWHM are being considered. On the other hand, by approximating the distribution to a ramp function, the events in the red region in figure 9 between z_1 and z_2 compensate for the lack of events in the green region of the same figure. Therefore, κ can be approximated by (3), where $f(z)$ corresponds to the function depicted in figure 9.

$$\kappa = \int_{z_2}^{z_6} f(z)\, dz \times \left(\int_{-\infty}^{+\infty} f(z)\, dz \right)^{-1} \tag{3}$$

Although (3) is the correct analytical expression for the aforementioned geometrical considerations, its implementation with real cases is not straightforward. Thus, it was decided to use for the integral in the numerator the z_1 and z_7 as limits of integration. It is assumed that any impact on the final result should be negligible given that there are very few events in this region with respect to the total number of events.

2.11. Systematic uncertainties

An estimation of the systematic uncertainties is crucial to obtain absolute yields. Although it is not possible to rule out other possible sources of systematic uncertainties, three main sources are assumed: (1) normalization with respect to the number of ions, (2) background subtraction procedure, and (3) geometrical description of each experimental setup. The systematic errors were rounded up to the next integer (in percentage) and they are shown on table 4. The systematic uncertainty shown in this table concerning background subtraction is a weighted average using the data points inside the ion range. It is the average of the absolute number of events left inside the TOF window after background subtraction weighted by the number of prompt gammas estimated after background subtraction. The calculation method of systematic uncertainty depends on the ion species and it is presented in section 2.11.2. Nevertheless, it should be noted that, for further analysis, each individual data point is assigned with a specific systematic uncertainty due to background subtraction and only one value is given in the aforementioned table for simplicity purposes.

Table 4. Estimated systematic uncertainties.

		Systematic uncertainty			
Experiment	Detector	Number of ions (%)	Background subtraction (%)	FOV (%)	Solid angle (%)
GANIL 95 MeV u^{-1} ^{12}C^{6+}	BaF$_2$	20	5	7	8
	NaI(Tl)	20	7	7	8
GSI 300 MeV u^{-1} ^{12}C^{6+}	BaF$_2$	10	14	8	9
GSI 310 MeV u^{-1} ^{12}C^{6+}	BaF$_2$	10	39	5	5
HIT 310 MeV u^{-1} ^{12}C^{6+}	LYSO:Ce	—	33	4	2
WPE 160 MeV H$^+$ (I)	LYSO:Ce	3	5	3	2
	LaBr$_3$:Ce	3	4	3	2
WPE 160 MeV H$^+$ (II)	LYSO:Ce	3	2	5	3
	LaBr$_3$:Ce	3	3	4	5
WPE 160 MeV H$^+$ (III)	LaBr$_3$:Ce	3	8	4	5

2.11.1. Number of ions. In order to retrieve the number of ions for posterior normalization, two methods were used in most of the experiments.

For the proton irradiation experiments, one method consisted of retrieving the number of particles by using the integrated current in the IC available at the beam nozzle and calibrated against a Bragg peak chamber detector. The other one used the MU system of the treatment system.

For the carbon ion cases, distinct approaches were applied in different experiments. For those at GANIL, a distant detector was calibrated using a Faraday cup. In the HIT 310 MeV u^{-1} ^{12}C^{6+} experiment and the ones at GSI, plastic scintillators were used, which also tagged the particle by yielding a TOF stop signal. In the experiments at GSI, a second method was implemented, consisting of an independent IC (i.e. plugged to a distinct electronics chain and acquisition system) calibrated by the plastic scintillators.

For all the experiments using two methods, only the results from one of them was used to normalise the data. The systematic error on the number of ions was assumed to be the maximum difference between the two methods considering all acquisition runs. Concerning the systematic error for the data from the GANIL experiments, the error on the calibration curve was used. For the HIT 310 MeV u^{-1} ^{12}C^{6+} experiment it was not possible to obtain an estimation of the systematic error on the number of ions since only one detector was used to retrieve the number of incident ions.

2.11.2. Background subtraction. As already detailed in section 2.9, two distinct background subtraction procedures were used according to the ion species. Consequently, different considerations were made to cope with the systematic error of each background subtraction method.

Carbon ion irradiation data. The rationale for subtracting the data of a given measurement with a reference TOF spectrum is to get a subtracted TOF spectrum in which only the prompt-gamma events are present. However, such a spectrum may be subjected to both statistical fluctuations and systematic uncertainties imparted by the method. If the method performs a good subtraction, all bins except the ones corresponding to prompt-gamma events should yield an average value of zero. Therefore, in order to estimate the systematic uncertainties of the method, the ten bins immediately before and after the TOF window for the prompt-gamma peak were used to make a linear fit and the contribution inside the TOF window was interpolated. The contribution of those events was compared with the total number of events inside

Table 5. Tolerances assumed for the geometrical description.

Geometrical element	Tolerance (mm)
Distance beam axis to collimator front face	±2.5
Distance collimator back face to detector	±2.5
Lead collimator thickness	±1.0
Tungsten collimator thickness	±0.25
Collimator slit with guide[a]	±0.1
Collimator slit without guide[a]	±1.0

[a] For all experiments, except for the GSI 300 MeV u^{-1} ^{12}C^{6+}, an aluminium piece was used along the slit to ensure a constant and fixed slit width.

the TOF window and this corresponds to the systematic uncertainties of the method. Only ten bins were used from each side because for some experiments the number of bins with meaningful data before the prompt-gamma peak is limited.

Proton irradiation data. The systematic uncertainty on the background subtraction method for proton irradiation data has been already described in section 2.9 and it is defined as the standard deviation of the number of counts retrieved by different approaches for background subtraction.

2.11.3. Experimental setup. From the systematic uncertainties considered, the ones related to the experimental setup are the most difficult to quantify. They are related to the accuracy of the measurements for each meaningful geometrical element in the experimental setup. The procedure was then to stipulate some reasonable assumptions related to the accuracy of the measurements and analytically estimate the change on the FOV and solid angle. After iterating along all possibilities considered for a given experiment, the maximum deviation was used as systematic uncertainty.

Monte Carlo simulations were not used to perform this estimation due to the CPU time needed. It is acknowledged that simulations are more accurate but the interest for this estimation is the variation yielded by changing geometrical dimensions rather than absolute values. The analytical procedure was verified with Monte Carlo simulations for the GSI 300 MeV u^{-1} ^{12}C^{6+} experiment. In this verification the slit width was varied and the difference in FOV and solid angle between simulations and the analytical approach was within ± 13%.

Table 5 presents the tolerance values considered for the geometrical dimensions. It should be stressed that some items are only applicable to specific experiments (e.g. the use of lead and tungsten collimators).

2.12. Absolute yields normalization

The absolute prompt-gamma yields $Y_{i, j}$ for a given experiment i and for a given longitudinal position along the target j in units of counts ion^{-1} mm^{-1} sr^{-1} are then obtained using (4) in which $S_{i, j}(t)$ corresponds to the TOF spectrum after subtraction for a given experiment i and longitudinal position j along the target, and N_{ions} to the estimated number of ions during the experiment. Variables κ, FOV, and ε_{att} are given in equations (1)–(3). The yields are estimated inside the TOF window $[t_1, t_2]$.

$$Y_{i,j} = \frac{\kappa}{N_{ions} \times \text{FOV} \times 4\pi\varepsilon_{att}} \times \int_{t_1}^{t_2} S_{i,j}(t) \, dt \qquad (4)$$
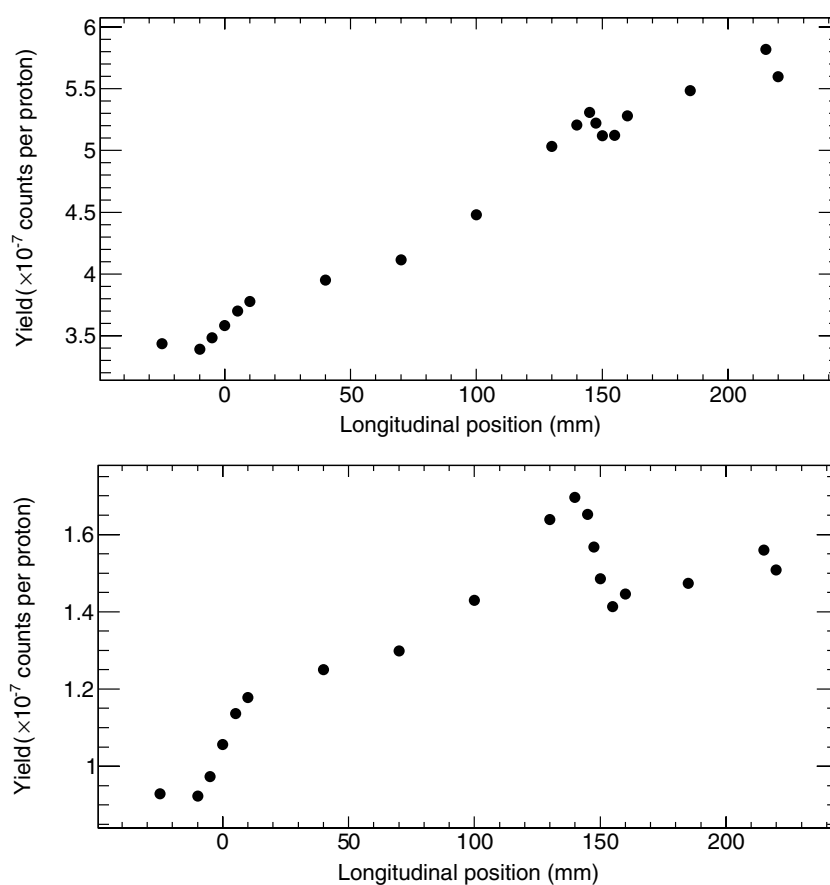
Figure 10. Profiles of the WPE 160 MeV H$^+$ (I) experiment, LaBr$_3$ detector, without using TOF (top) and using TOF (bottom). The error bars are of the same size as the symbols and correspond only to statistical uncertainties (one standard deviation).

3. Results

There are in total ten experimental cases being considered in this work. In each subsection only typical cases for both proton and carbon ion experiments are presented.

3.1. Experimental analysis

Figures 10 and 11 show the prompt-gamma profiles with and without TOF selection for proton and carbon ion experiments, respectively. The TOF selection window for each case corresponds to the values presented in table 1.

Among the proton experiments, applying TOF selection enhances the signal to background ratio of the prompt-gamma profile, making the fall-off more prominent. In turn, in the data from carbon ion experiments, it is not possible to observe the prompt-gamma profile fall-off next to the end of the ion range unless TOF is used.
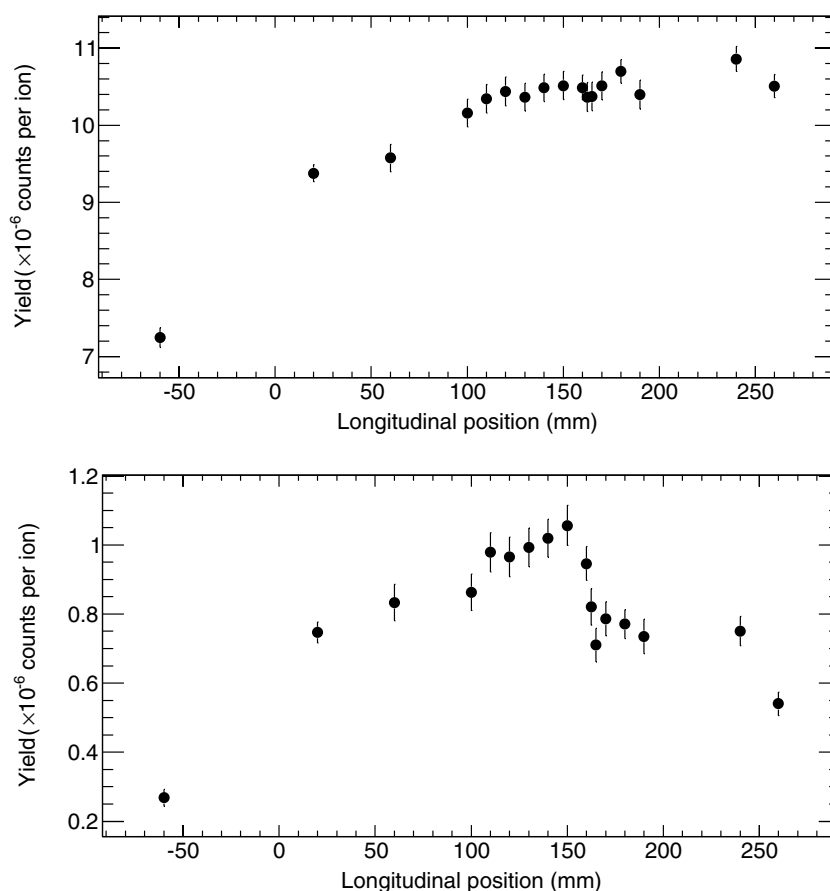
Figure 11. Profiles of the HIT 310 MeV u^{-1} ^{12}C^{6+} experiment, LYSO detector, without using TOF (top) and using TOF (bottom). The error bars correspond only to statistical uncertainties (one standard deviation).

3.2. Background subtraction

3.2.1. Carbon ion irradiation data. Herein the steps of the background subtraction procedure for the carbon ion data are shown for the GSI 300 MeV u^{-1} ^{12}C^{6+} experiment as an example. In figure 12 (top) two TOF spectra are depicted, the reference spectrum and the one that will undergo the background subtraction (measurement at 160 mm inside the target). Afterwards, in figure 12 (middle) the reference spectrum is scaled using a factor based on the integral outside the TOF window for both spectra in order to account for the difference in background magnitude. The spectrum at a given position is then subtracted using the scaled reference TOF spectrum. Finally, in figure 12 (bottom) the TOF region around the prompt-gamma peak after background subtraction is shown along with the linear fit used to estimate the systematic uncertainty on the background subtraction procedure. For this specific case it can be observed that the systematic uncertainty is relatively small since the linear fit obtained with the points around the prompt-gamma peak is almost constant and equal to zero.
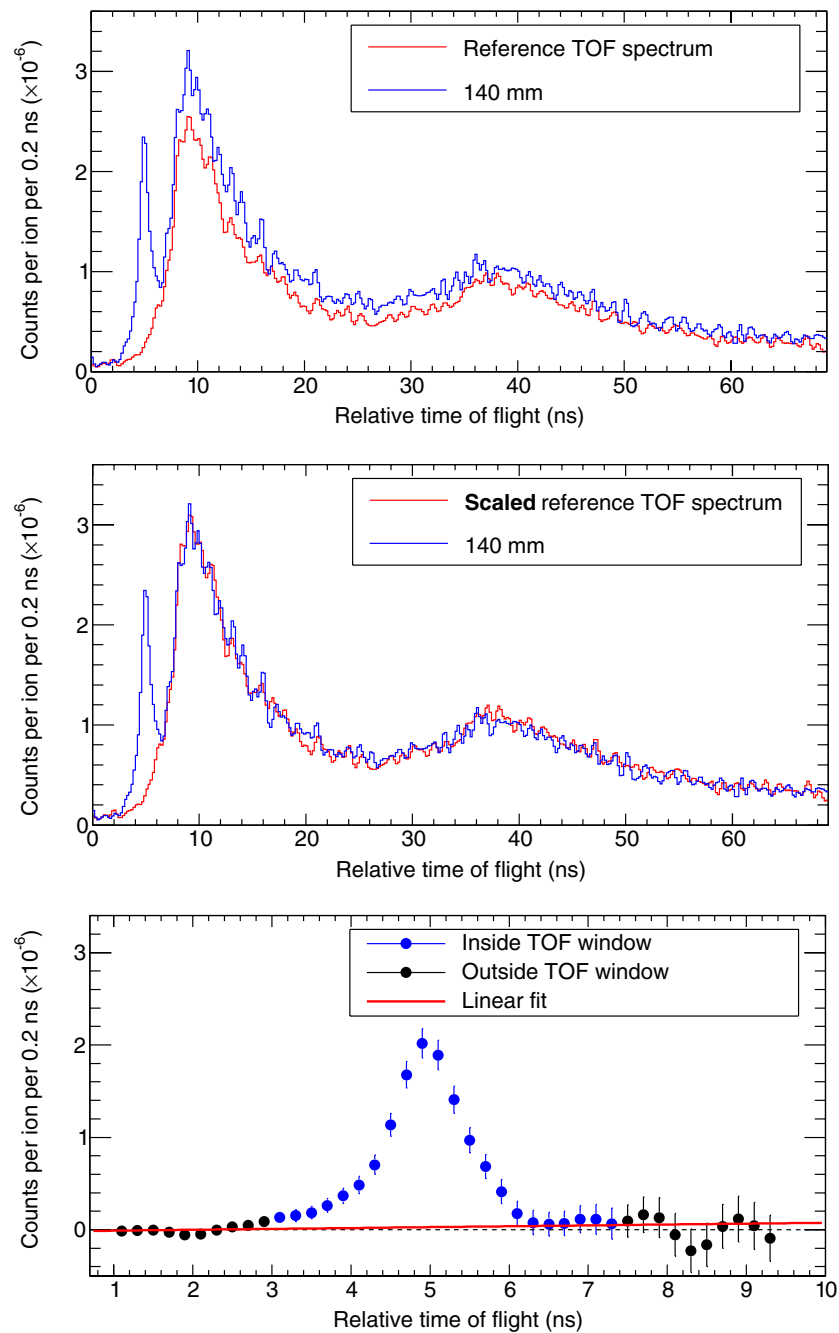
Figure 12. Different steps of the background subtraction procedure using the GSI 300 MeV u^{-1} ^{12}C^{6+} experiment and the measurement at 140 mm inside the target as an example. Top: TOF spectrum to be subtracted and the reference one. Middle: reference TOF spectrum scaled in order to account for the difference in background magnitude. Bottom: TOF region around the prompt-gamma peak after background subtraction.
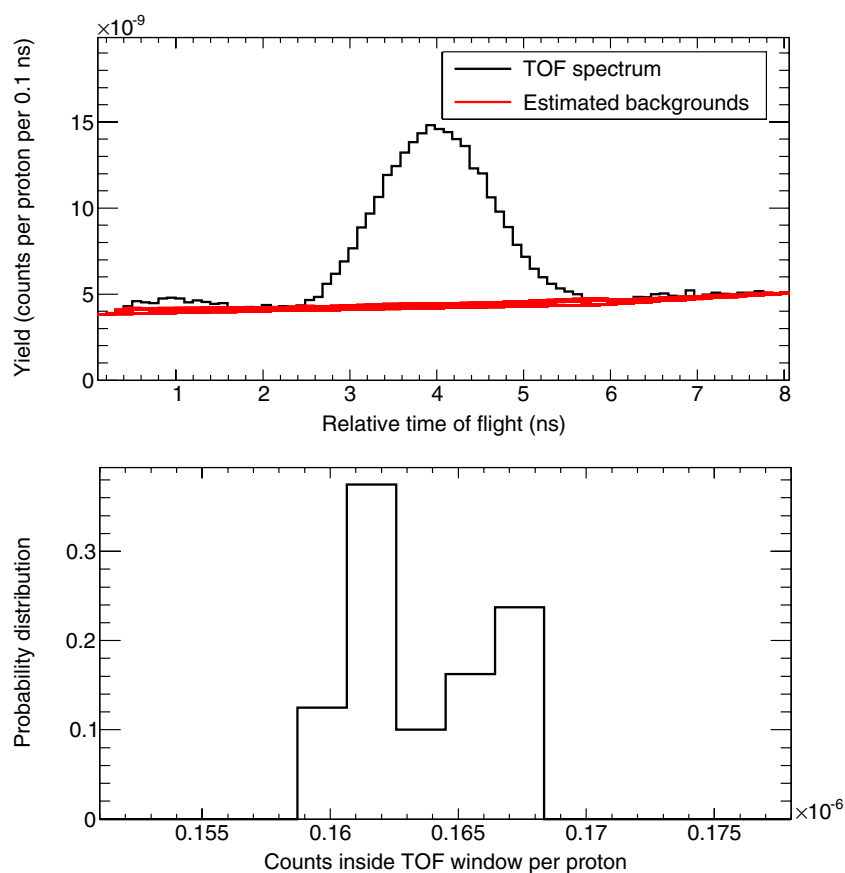
Figure 13. Top: example of a TOF spectrum undergoing subtraction for the WPE 160 MeV H$^+$ (II) experiment using the LYSO detector. The background estimation was performed using the ROOT routine TSpectrum and all estimated backgrounds for this specific case by such a routine are depicted in the figure. Bottom: distribution of integral values inside the TOF window retrieved after the application of the TSpectrum routine with different parameters. For this specific case, the average value and the standard deviation are, respectively, 0.163×10^{-6} and 0.003×10^{-6} counts inside TOF window per incident proton.

3.2.2. Proton irradiation data. Concerning the proton experiments, the TSpectrum routine was used in order to estimate the background superimposed with the prompt-gamma peak. figure 13 (top) depicts one case for which the aforementioned routine estimates the background based on some initial parameters. The routine is repeatedly applied with different initial parameters and the number of events inside the TOF window for each case is used to produce a distribution like the one shown in figure 13 (bottom). The average value is considered as the number of prompt gammas inside the TOF window and the standard deviation of such a distribution is imparted to the results as systematic uncertainty.

3.3. Geometrical normalization

Each experiment was simulated and the FOV, ε and κ were estimated. Figure 14 depicts some of the profiles used to estimate the FOV and κ and table 6 contains the outcomes of this analysis for all experiments.
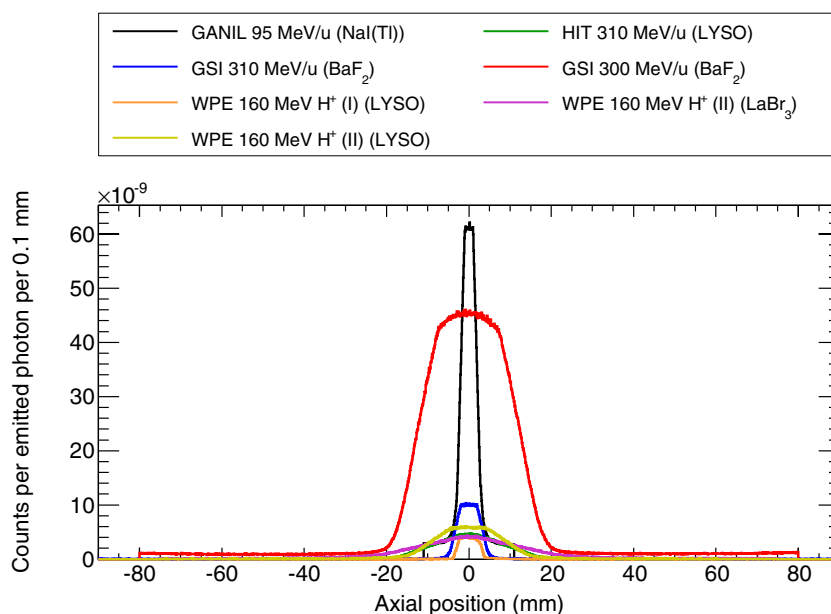
Figure 14. Simulated profiles used to estimate the FOV and κ. Each profile represents the emission axial position of a gamma that had an energy deposition inside the detector between 1 and 7 MeV. The profiles of some experiments are omitted since they are similar to, at least, one of the depicted.

Table 6. Geometrical normalization of the data. The percent difference in the ε_{att} column refers to the difference with respect to the ε value.

Experiment	Detector	FOV (mm)	ε ($\times 10^{-6}$)	ε_{att} ($\times 10^{-6}$)	κ
GANIL 95 MeV u^{-1} ^{12}C^{6+}	BaF$_2$	4.3	48	44 (-8%)	0.80
	NaI(Tl)	4.2	28	26 (-7%)	0.83
GSI 300 MeV u^{-1} ^{12}C^{6+}	BaF$_2$	25.1	215	187 (-13%)	0.90
GSI 310 MeV u^{-1} ^{12}C^{6+}	BaF$_2$	6.7	54	45 (-17%)	0.90
HIT 310 MeV u^{-1} ^{12}C^{6+}	LYSO	20.0	21	18 (-14%)	0.92
WPE 160 MeV H$^+$ (I)	LaBr$_3$	7.5	14	11 (-21%)	0.95
	LYSO	6.0	15	12 (-20%)	0.94
WPE 160 MeV H$^+$ (II)	LaBr$_3$	27.1	16	13 (-19%)	0.84
	LYSO	19.3	22	18 (-18%)	0.89
WPE 160 MeV H$^+$ (III)	LaBr$_3$	27.1	16	13 (-19%)	0.84

3.4. Absolute yields

After estimating the geometrical factors and the prompt-gamma signal from the background subtraction, it is possible to obtain the absolute yields for each experiment for both proton (figure 15) and carbon ion (figure 16) data set. The error bars presented in the profiles include both statistical (one standard deviation) and systematic uncertainties after a quadratic sum.

The results gathered from both figures 15 and 16 are shown in table 7. In order to avoid the pile-up of events coming from secondary particles increasingly produced downstream along the beam path with the ones originated from incident ions, the results presented use the data from the first measured point inside the target not affected by the prompt-gamma profile
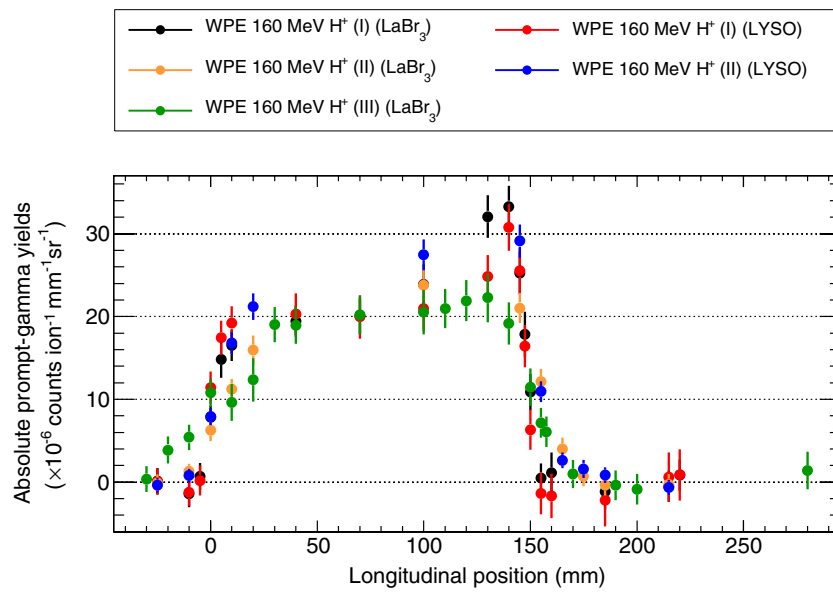
Figure 15. Profiles of the proton experiments after full normalization. Each data point includes both statistical (one standard deviation) and the considered systematic uncertainties.

Figure 16. Profiles of the carbon ion experiments after full normalization. Each data point includes both statistical (one standard deviation) and the cons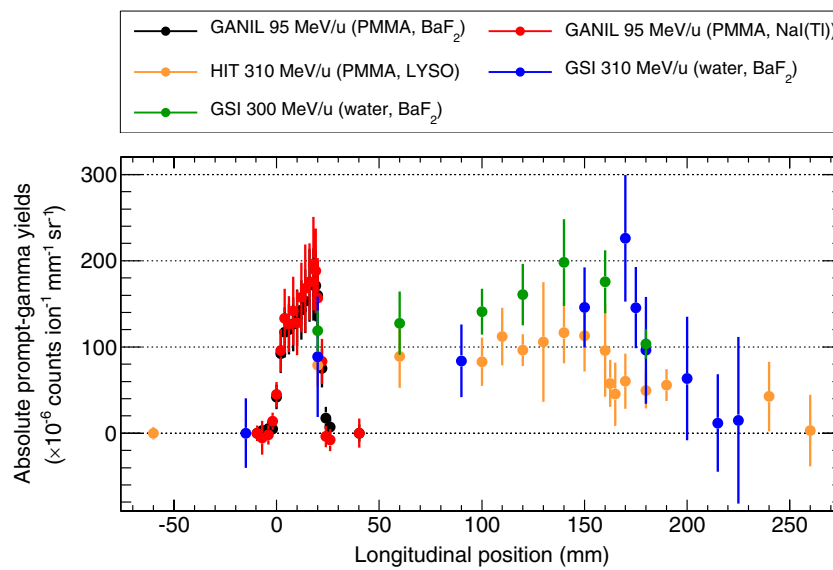idered systematic uncertainties. The length of the target used in a given experiment is represented by the box on the bottom of the figure with the same colour as the one of the markers of the respective experimental profile.

Table 7. Absolute yields using the first measured point inside the target not affected by the prompt-gamma profile entrance rise (see figure 17) with both statistical and systematic uncertainties. The energy range row shows the energy range of the primary particles inside the FOV of the first point after the target entrance estimated by Geant4 (see figure 17). When the results of more than one experiment are combined, the energy range considers the maximum energy limits amongst all the experiments considered.

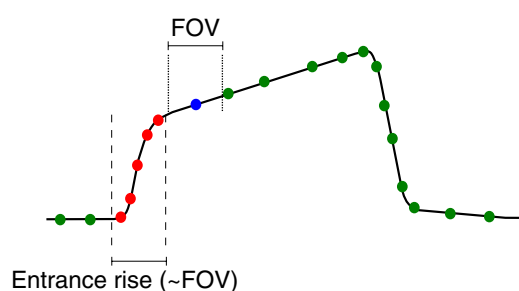| Material	Energy range (MeV u^{-1})	Ion species	Absolute yield ($\times 10^{-6}$ counts ion^{-1} mm^{-1} sr^{-1})
PMMA	[77–90]	Carbon ions	$124 \pm 0.7_{stat} \pm 30_{sys}$
PMMA	[272–310]	Carbon ions	$79 \pm 2_{stat} \pm 23_{sys}$
Water	[264–292]	Carbon ions	$112 \pm 1_{stat} \pm 22_{sys}$
PMMA	[139–156]	Protons	$16 \pm 0.07_{stat} \pm 1_{sys}$

Figure 17. Schematic representation of a hypothetical prompt-gamma profile in order to explain the selection of the point used to estimate the absolute yields presented in table 7. The point used is the first measurement position after the entrance rise (blue circle). It also depicts the points comprising the entrance rise (red circles) and the other data points (green circles). In addition, the FOV of the considered data point for the yield estimation is shown. The energy range of the beam particles within these boundaries is estimated with Geant4 and presented in table 7.

entrance rise (i.e. after half FOV centred at target entrance, see figure 17 for additional details). This assumption was verified with Geant4 (using reference physics list QGSP_BIC_HP) and it was found that for all carbon ion experiments, at least 90% of the particles at the point considered are primary particles (electrons are disregarded). For the proton irradiation, this percentage is of at least 97%.

For the cases where there is data from more than one experiment, the standard weighted least-squares formula (Beringer *et al* 2012) is used. Only statistical uncertainties are considered for error propagation. Regarding the systematic uncertainties, most of them should be correlated at some extent but their error propagation proved to be extremely difficult. As such, when results are combined in any way and systematic uncertainties are stated, it was decided to use the largest systematic uncertainty amongst all results to be combined.

4. Discussion

Following the findings of Testa *et al* (2008), all data analyses here presented were based on the TOF spectrum analysis of the different experiments. Indeed, the use of TOF has proven to be an efficient way to discriminate prompt gammas (i.e. signal) from neutrons and neutron-induced

gammas (i.e. background). Such findings can be observed and confirmed in figures 10 and 11, which show that TOF allows for yielding an improved description of the fall-off in the prompt-gamma longitudinal profile close to the expected position of the Bragg peak fall-off. It was also shown by Roellinghoff *et al* that its application improves the precision in finding the proton range in prompt-gamma monitoring by enhancing the SBR (Roellinghoff *et al* 2014).

Absolute prompt-gamma yields are presented in this study. They include both statistical and systematic uncertainties. Although it is not possible to rule out other sources of systematic uncertainties, the ones considered should have the highest impact. To some extent, the good agreement for both proton and carbon ion irradiation found among different experimental conditions (i.e. targets, detectors, setup geometries, facilities, and energy in the case of carbon ions) acts as a validation of the results. For the proton case, the same energy and target composition is used, thus the same absolute yields are expected. For the carbon ion experiments, each type of experiment (lower and higher energy) follows the trend published by Kox *et al* (1987), which shows a total reaction cross sections for ^{12}C–^{12}C experiments of 965 mb and 858 mb for 83 and 300 MeV u^{-1} projectile energy, respectively. Assuming a similar trend for the present cases, the lower energy experiments should express an increased prompt-gamma emission, which is actually verified. Moreover, the results show a higher prompt-gamma emission when using a water target with respect to a PMMA one (*vide* e.g. table 7 for the two highest energy ranges of carbon ions). It has been suggested that the target composition plays an important role in the prompt-gamma emission for proton irradiation, namely on the oxygen content (Polf *et al* 2013). The present work shows the same tendency when irradiating with carbon ions since the absolute yield with the PMMA target was lower than the one with the water target (a factor of $0.71 \pm 0.02_{stat} \pm 0.25_{sys}$).

Comparing the prompt-gamma yields of two different ion species with the same range in water, i.e. 160 MeV protons and 310 MeV u^{-1} carbon ions, the latter shows a value about five times greater than the former. Although there was no clear idea about how much the yield for carbon ions would be, the increased emission is expected since in a carbon ion irradiation both target nuclei and projectile contribute for such an emission, while in a proton irradiation only the target nuclei may emit prompt gammas.

Recently Agodi *et al* (2013) published prompt-gamma absolute yields of 80 MeV u^{-1} carbon ions impinging on a PMMA target. They found a yield of $(2.32 \pm 0.01_{stat} \pm 0.15_{sys}) \times 10^{-3}$ counts ion^{-1} sr^{-1} for energies above 2 MeV and considering the full ion range. The comparison between the results presented herein and the aforementioned study is not direct since some considerations must be applied. Only the results of the GANIL 95 MeV u^{-1} experiment are suitable for such a comparison due to the similar energy range. However, the results shown in table 7 only consider a point after the entrance with a single-slit collimator while Agodi *et al* published the integrated emission for the entire ion range. As such, if an average value between the entrance and the maximum yield immediately upstream of the prompt-gamma falloff is used, conditioned by a 2 MeV energy threshold (i.e. all steps described in the present work are repeated with 2 MeV as lower energy threshold instead of 1 MeV), an absolute yield of $(174 \pm 0.9_{stat} \pm 50_{sys}) \times 10^{-6}$ counts ion^{-1} mm^{-1} sr^{-1} is obtained. The corresponding value published by Agodi and colleagues after considering the projected ion range of 80 MeV u^{-1} carbon ions in PMMA (15.42 mm, estimated with SRIM 2013) is $(150 \pm 0.6_{stat} \pm 10_{sys}) \times 10^{-6}$ counts ion^{-1} mm^{-1} sr^{-1}. Although the outcome from our collaboration suffers from a higher systematic uncertainty, the agreement with previously published results from independent collaborations is remarkably good. Further experiments aiming at confirming these results with lower systematic uncertainties may provide additional information.

The outcomes presented herein use the data from two experiments already published by our collaboration (Le Foulher *et al* 2010, Testa *et al* 2010). The present study provides slightly different results from the ones that can be found in those articles. Such a difference is the

Table 8. Number of prompt gammas estimated using the absolute yields shown in table 7 and taking into account the number of ions used for two treatment scenarios.

		Number of prompt gammas (counts mm^{-1} sr^{-1})
Protons	Spot	$800 \pm 4_{stat} \pm 50_{sys}$
	Energy slice	$36\,800 \pm 161_{stat} \pm 2300_{sys}$
Carbon ions	Spot	$8 \pm 0.2_{stat} \pm 2_{sys}$
	Energy slice	$790 \pm 20_{stat} \pm 230_{sys}$

consequence of a review process of most of our single-slit collimator data, namely in terms of background subtraction methods, dead time correction and error estimation. Therefore, the results presented here should be seen as an updated and more accurate set of data and should be considered instead.

Finally, it is possible to use the experimental results to make some considerations about prompt-gamma monitoring in a treatment scenario. For proton irradiation, and based on other studies (Smeets *et al* 2012, Gueth *et al* 2013) in which the number of protons for a given spot used for a prostate tumour treatment is considered, it was decided to use 5×10^7 protons per spot and 46 spots per energy slice. On the other hand, Krämer *et al* (2000) states a total of 7×10^8 carbon ions in the target volume (around 120 cm^3) to deliver an absorbed dose of 1 Gy using around 10 000 raster positions with 39 energy slices. Hence, as an approximation, 1×10^5 and 1×10^7 carbon ions will be considered in this analysis, respectively per spot and per energy slice. Table 8 shows the extrapolation of the absolute yields in table 7 to a given treatment scenario in the aforementioned conditions, considering the PMMA target for both cases, and using the data from the higher energy carbon ion irradiation.

On the other hand, a precise estimation concerning the background events in a treatment scenario may be extremely difficult with the available data. The number of background events depends on, for example, the treatment room dimensions and materials, the specifications of the monitoring camera (namely the collimating and detection devices), and the beam time structure (e.g. if the particle bunches have a sufficiently large period, the background events originated after one particle bunch will not overlap with the prompt-gamma events of the next one). Moreover, it is not possible to simply apply the normalization factors used to obtain the absolute prompt-gamma emission yields to background events, since all the assumptions rely on prompt-gamma interactions. However, one can extrapolate the background events observed in the experimental data and infer some conclusions concerning those in a treatment scenario. As described before, the number of prompt-gamma events is obtained through the integration of the events inside the time window after background subtraction. In turn, the background events can be estimated by subtracting the number of prompt-gamma events from the integral inside the time window before background subtraction. Using the experimental data from the HIT 310 MeV u^{-1} ^{12}C^{6+} and the WPE 160 MeV H$^+$ (II) with the LYSO:Ce detector experiments, respectively for carbon ions and protons, it is possible to retrieve a ratio of prompt-gamma to background events inside the TOF window and it was found to be around 1 : 1. Assuming that the same relationship holds for a treatment scenario and for a full-size camera, these results associated with the ones from table 8 unequivocally demonstrate the feasibility of discriminating the prompt-gamma signal from the background. Indeed, the number of prompt gammas is always at least 3σ of the background statistical fluctuations, except for the case of monitoring a carbon ion treatment at spot level. In fact, the aforementioned situation is the only one that poses more challenges due to the low signal available.

5. Conclusions

Herein an extensive study of the data from ten single-slit experiments, involving either proton or carbon ion irradiation, PMMA or water targets, and different geometries, was undertaken in order to obtain absolute prompt-gamma yields. Such results are of utmost importance for the research and development of hadrontherapy monitoring solutions based on prompt gammas. On the one hand, these yields can now be used for Monte Carlo tools assessment, by comparison with the simulation outcome concerning prompt-gamma emission. On the other hand, they can also be used to estimate the expected performance of any monitoring device since they are normalized to the geometrical definition of the different experiments.

At the entrance of a PMMA target, where the contribution of secondary nuclear reactions is negligible, prompt-gamma counts per incident ion, per millimetre and per steradian equal to $(124 \pm 0.7_{stat} \pm 30_{sys}) \times 10^{-6}$ for 95 MeV u^{-1} carbon ions, $(79 \pm 2_{stat} \pm 23_{sys}) \times 10^{-6}$ for 310 MeV u^{-1} carbon ions, and $(16 \pm 0.07_{stat} \pm 1_{sys}) \times 10^{-6}$ for 160 MeV protons were found for prompt gammas with energies higher than 1 MeV. For water targets and high energy carbon ions (300 and 310 MeV u^{-1}) the yield obtained was $(112 \pm 1_{stat} \pm 22_{sys}) \times 10^{-6}$ counts ion^{-1} mm^{-1} sr^{-1}.

The difference between the yields of 310 MeV u^{-1} carbon ions and 160 MeV protons, two different ion species with equivalent range in water, was found to be a factor 5 (greater yield for the carbon ion). Moreover, among the two groups of carbon ion energies, an increased prompt-gamma emission is verified for the lowest energy group as expected from published ^{12}C–^{12}C cross sections.

Concerning the influence of the target material in the prompt-gamma yields, it was found, for 300 and 310 MeV u^{-1} carbon ions, that a water target results in a 42% higher yield with respect to a PMMA target. Nevertheless, further studies are essential to quantify the importance of the target material composition in the prompt-gamma yields.

Finally, the extrapolation of the results obtained for a treatment scenario shows the feasibility of prompt-gamma monitoring for hadrontherapy, namely in terms of the amount of signal and the ability to discriminate prompt-gamma events from background. The only situation for which some doubts persist is the carbon-ion therapy monitoring at the spot level. For this case with the treatment plan considered, only 8 counts mm^{-1} sr^{-1} are emitted. In turn, the number of background events registered in the experimental data was found to be approximately a 1 : 1 correspondence to the number of detected prompt gammas. This allows for discriminating prompt gammas from background fluctuations at relatively low number of counts. Moreover, the background subtraction procedure based on the TOF information presented herein (for which measurements upstream of the target are performed), or an alternative one, may be implemented in a clinical device. Hence, this would inevitably allow for a maximisation of the contrast on the prompt-gamma signal with a potential impact on the monitoring precision that could reflect on better monitoring outcomes.

Appendix A. Summary of the experiments

Table A1. Summary of the features of the targets, detectors and collimators used in each experiment.

	Carbon-ion experiments			
	GANIL 95 MeV u^{-1}	GSI 300 MeV u^{-1}	GSI 310 MeV u^{-1}	HIT 310 MeV u^{-1}
Target-detector Distance (mm)	605	990	1345	635
Target material	PMMA	Water	Water	PMMA
Target Longitudinal Dimension (mm)	54	200	200	250
Target Transversal Dimensions (mm^2)	50 × 50	120 × 250	120 × 250	100 × 100
Detector	BaF$_2$ NaI(Tl)	BaF$_2$	BaF$_2$	LYSO:Ce
Collimator material	Lead	Lead	Lead	Tungsten
Collimator Thickness (mm)	200	200	200	100
Collimator slit (mm)	2	15	4	4

	Proton experiments		
	WPE		
	160 MeV (I)	160 MeV (II)	160 MeV (III)
Target-detector Distance (mm)	600	505	505
Target material	PMMA	PMMA	PMMA
Target Radius (mm)	75	75	75
Target Length (mm)	200	200	250
Detector	LYSO:Ce LaBr$_3$:Ce	LYSO:Ce LaBr$_3$:Ce	LaBr$_3$:Ce
Collimator material	Tungsten	Tungsten	Tungsten
Collimator Thickness (mm)	100	100	100
Collimator slit (mm)	4	4	4

References

Agodi C *et al* 2012 Precise measurement of prompt photon emission from 80 MeV u^{-1} carbon ion beam irradiation *J. Instrum.* **7** P03001

Agodi C *et al* 2013 Erratum: precise measurement of prompt photon emission from 80 MeV u^{-1} carbon ion beam irradiation *J. Instrum.* **8** E11002

Agostinelli S *et al* 2003 Geant4: a simulation toolkit *Nucl. Instrum. Methods* A **506** 250–303

Amaldi U, Hajdas W, Iliescu S, Malakhov N, Samarati J, Sauli F and Watts D 2010 Advanced quality assurance for CNAO *Nucl. Instrum. Methods* A **617** 248–9

Bauer J, Unholtz D, Sommerer F, Kurz C, Haberer T, Herfarth K, Welzel T, Combs S E, Debus J and Parodi K 2013 Implementation and initial clinical experience of offline PET/CT-based verification of scanned carbon ion treatment *Radiother. Oncol.* **107** 218–26 (www.sciencedirect.com/science/article/pii/S0167814013001606)

Beringer J *et al* 2012 Review of particle physics *Phys. Rev.* D **86** 010001

Biegun A K *et al* 2012 Time-of-flight neutron rejection to improve prompt gamma imaging for proton range verification: a simulation study *Phys. Med. Biol.* **57** 6429

Bom V, Joulaeizadeh L and Beekman F 2012 Real-time prompt gamma monitoring in spot-scanning proton therapy using imaging through a knife-edge-shaped slit *Phys. Med. Biol.* **57** 297

Brun R and Rademakers F 1997 ROOT: an object oriented data analysis framework *Nucl. Instrum. Methods* A **389** 81–6 (www.sciencedirect.com/science/article/pii/S016890029700048X)

Enghardt W, Crespo P, Fiedler F, Hinz R, Parodi K, Pawelke J and Pönisch F 2004 Charged hadron tumour therapy monitoring by means of PET *Nucl. Instrum. Methods* A **525** 284–8

Golnik C *et al* 2014 Range assessment in particle therapy based on prompt γ-ray timing measurements *Phys. Med. Biol.* **59** 5399

Grevillot L, Bertrand D, Dessy F, Freud N and Sarrut D 2011 A Monte Carlo pencil beam scanning model for proton treatment plan simulation using GATE/GEANT4 *Phys. Med. Biol.* **56** 5203

Gueth P, Dauvergne D, Freud N, Létang J M, Ray C, Testa E and Sarrut D 2013 Machine learning-based patient specific prompt-gamma dose monitoring in proton therapy *Phys. Med. Biol.* **58** 4563

Gunzert-Marx K, Iwase H, Schardt D and Simon R S 2008 Secondary beam fragments produced by 200 MeV u^{-1} ^{12}C ions in water and their dose contributions in carbon ion radiotherapy *New J. Phys.* **10** 075003

Henriquet P *et al* 2012 Interaction vertex imaging (IVI) for carbon ion therapy monitoring: a feasibility study *Phys. Med. Biol.* **57** 4655

Hishikawa Y, Kagawa K, Murakami M, Sakai H, Akagi T and Abe M 2002 Usefulness of positron-emission tomographic images after proton therapy *Int. J. Radiat. Oncol. Biol. Phys.* **53** 1388–91 (www.sciencedirect.com/science/article/pii/S0360301602028870)

Kim D, Yim H and Kim J W 2009 Pinhole camera measurements of prompt gamma-rays for detection of beam range variation in proton therapy *J. Korean Phys. Soc.* **55** 1673–6

Knopf A C and Lomax A 2013 *In vivo* proton range verification: a review *Phys. Med. Biol.* **58** R131

Kormoll T, Fiedler F, Schöne S, Wüstemann J, Zuber K and Enghardt W 2011 A Compton imager for *in-vivo* dosimetry of proton beams-a design study *Nucl. Instrum. Methods* A **626–7** 114–9 (www.sciencedirect.com/science/article/pii/S0168900210022709)

Kox S *et al* 1987 Trends of total reaction cross sections for heavy ion collisions in the intermediate energy range *Phys. Rev.* C **35** 1678–91

Krämer M, Jäkel O, Haberer T, Kraft G, Schardt D and Weber U 2000 Treatment planning for heavy-ion radiotherapy: physical beam model and dose optimization *Phys. Med. Biol.* **45** 3299

Le Foulher F *et al* 2010 Monte Carlo simulations of prompt-gamma emission during carbon ion irradiation *IEEE Trans. Nucl. Sci.* **57** 2768–72

Lee H R, Park J H, Kim C H and Min C H 2012 Design optimization of a 2d prompt-gamma measurement system for proton dose verification *J. Korean Phys. Soc.* **61** 239–42

Min C H, Kim C H, Youn M Y and Kim J W 2006 Prompt gamma measurements for locating the dose falloff region in the proton therapy *Appl. Phys. Lett.* **89** 183517

Morháč M, Kliman J, Matoušek V, Veselský M and Turzo I 1997 Background elimination methods for multidimensional coincidence γ-ray spectra *Nucl. Instrum. Methods* A **401** 113–32 (www.sciencedirect.com/science/article/pii/S0168900297010231)

España S E, Zhu X, Daartz J, Fakhri G E, Bortfeld T and Paganetti H 2011 The reliability of proton-nuclear interaction cross-section data to predict proton-induced PET images in proton therapy *Phys. Med. Biol.* **56** 2687

Park J H, Seo H, Kim Y S, Kim C H, Lee J H, Lee C S, Kim S M and Lee J S 2012 Monte Carlo simulations on performance of double-scattering compton camera *J. Instrum.* **7** C01009

Parodi K *et al* 2007 Patient study of *in vivo* verification of beam delivery and range, using positron emission tomography and computed tomography imaging after proton therapy *Int. J. Radiat. Oncol. Biol. Phys.* **68** 920–34 (www.sciencedirect.com/science/article/pii/S036030160700377X)

Peterson S W, Robertson D and Polf J 2010 Optimizing a three-stage compton camera for measuring prompt gamma rays emitted during proton radiotherapy *Phys. Med. Biol.* **55** 6841

Pinto M, Dauvergne D, Freud N, Krimmer J, Letang J, Ray C, Roellinghoff F and Testa E 2014 Design optimisation of a TOF-based collimated camera prototype for online hadrontherapy monitoring *Phys. Med. Biol.* **59** 7653–74

Polf J C, Mackin D, Lee E, Avery S and Beddar S 2014 Detecting prompt gamma emission during proton therapy: the effects of detector size and distance from the patient *Phys. Med. Biol.* **59** 2325

Polf J C, Panthi R, Mackin D S, McCleskey M, Saastamoinen A, Roeder B T and Beddar S 2013 Measurement of characteristic prompt gamma rays emitted from oxygen and carbon in tissue-equivalent samples during proton beam irradiation *Phys. Med. Biol.* **58** 5821

Richard M H *et al* 2011 Design guidelines for a double scattering compton camera for prompt-γ imaging during ion beam therapy: a Monte Carlo simulation study *IEEE Trans. Nucl. Sci.* **58** 87–94

Robert C *et al* 2013 Distributions of secondary particles in proton and carbon-ion therapy: a comparison between GATE/Geant4 and FLUKA monte carlo codes *Phys. Med. Biol.* **58** 2879

Robertson D, Polf J C, Peterson S W, Gillin M T and Beddar S 2011 Material efficiency studies for a Compton camera designed to measure characteristic prompt gamma rays emitted during proton beam radiotherapy *Phys. Med. Biol.* **56** 3047

Roellinghoff F *et al* 2014 Real-time proton beam range monitoring by means of prompt-gamma detection with a collimated camera *Phys. Med. Biol.* **59** 1327

Schardt D, Elsässer T and Schulz-Ertner D 2010 Heavy-ion tumor therapy: physical and radiobiological benefits *Rev. Mod. Phys.* **82** 383–425

Seravalli E *et al* 2012 Monte Carlo calculations of positron emitter yields in proton radiotherapy *Phys. Med. Biol.* **57** 1659

Smeets J *et al* 2012 Prompt gamma imaging with a slit camera for real-time range control in proton therapy *Phys. Med. Biol.* **57** 3371

Testa E, Bajard M, Chevallier M, Dauvergne D, Foulher F L, Freud N, Letang J M, Poizat J C, Ray C and Testa M 2008 Monitoring the Bragg peak location of 73 MeV u^{-1} carbon ions by means of prompt gamma-ray measurements *Appl. Phys. Lett.* **93** 093506

Testa E, Bajard M, Chevallier M, Dauvergne D, Foulher F L, Freud N, Letang J, Poizat J, Ray C and Testa M 2009 Dose profile monitoring with carbon ions by means of prompt-gamma measurements *Nucl. Instrum. Methods* B **267** 993–6

Testa M *et al* 2010 Real-time monitoring of the Bragg-peak position in ion therapy by means of single photon detection *Radiat. Environ. Biophys.* **49** 337–43

Verburg J M, Riley K, Bortfeld T and Seco J 2013 Energy- and time-resolved detection of prompt gamma-rays for proton range verification *Phys. Med. Biol.* **58** L37

Verburg J M, Shih H A and Seco J 2012 Simulation of prompt gamma-ray emission during proton radiotherapy *Phys. Med. Biol.* **57** 5459

Ziegler J, Biersack J and Ziegler M 2008 *SRIM, the Stopping and Range of Ions in Matter* (Maryland: SRIM Company)